

(*掲載記事題目及び掲載頁は変更になる場合があります。*)

Mechanical Properties

Macroscopic stress measurements by neutron diffraction and the part played by the "stress-free" reference (Review)

T.M.HOLDEN *et al.*

In the last decade a more sophisticated understanding of how to calculate the macroscopic stress from strains measured in neutron diffraction experiments has developed. Strains measured with the aid of a particular reflection may have a component corresponding to the stress field as well as a component corresponding to a type-2 or intergranular stress. The latter originates in inhomogeneous plastic deformation among different grain orientations. One approach is to cut small reference coupons from the component, small in size compared with the variation of the stress field. Cutting destroys the stress field but leaves any chemistry and intergranular effects intact since they are on the scale of the grain size. The difference between the intact sample and the coupon then gives an approximation to the strain associated with the macroscopic stress.

Examples of how the intergranular and macroscopic strains and stresses are superposed, are presented for the cases of slightly bent and severely bent steam generator tubing, and for a deformed pressure tube. Welds often represent a situation where plastic deformation has occurred on cooling. In addition, microstructural and compositional changes are often associated with melting, so it is important to have reference coupons as a function of position through the weld zone. Examples of austenitic stainless steel and Zr-alloy welds are presented where this procedure was followed.

(cf. *ISIJ Int.*, **46** (2006), 959)

Fundamentals of High Temperature Processes

Predicting the chromite mineral upgradation in floatex density separator using hindered settling models

C.KARI *et al.*

Floatex density separator is a commercial hindered (teetered) bed separator and works on the principle of hindered settling. In hindered settling, prediction of the separation behaviour of mineral particles is complex and challenging, since the settling velocities of the particles are influenced by the nearby particles. In the present work, empirical hindered settling models available in literature have been successfully used for predicting the separation of chromite mineral in liquid fluidized bed created in Floatex Density separator (FDS) unit for the first time. Two hindered settling models have been used for predicting the performance of the FDS unit in terms of the weight recoveries and the mineral composition of the FDS underflow product. This predicted data is validated using the experimental data generated from three different random plant scale trials with FDS unit. The agreement between the results predicted from the model are found to be match with the experimental results with less than 5% error at low suspension densities and low teeter water velocities upto 25 mm/s. Therefore, the mod-

els have been further explored to study the effect of teeter water velocity on the chromite grade and overall chromite metal recoveries within the model applicable range of teeter-water velocities. This has resulted in a fair amount of understanding of the separation behaviour of the chromite mineral in FDS and helped in choosing the operating parameters for production of desired grades of chrome concentrate as FDS underflow. Hence, the value of this paper is in its validation of simple hindered settling models and their application to predict recoveries and upgradation of chromite ore at industrial scale.

(cf. *ISIJ Int.*, **46** (2006), 966)

Oxygen exchange reaction between CO₂-CO gas and molten oxide containing iron oxide

X.HU *et al.*

Oxygen exchange reaction rates between CO₂-CO gas and molten oxides containing iron oxide have been measured by isotope exchange technique with ¹⁸O at 1 773 K with $P_{CO_2}/P_{CO}=1$. Measured results represent that the oxygen exchange reaction rates show the maximum values at the beginning of the reaction and sharply decrease within approximately 20 s, and then gradually decrease with the reaction time proceeds. These changes indicate that the rate-limiting step would change from the dissociative adsorption of oxygen on the surface of molten oxide in the initial stage of reaction to the mass transfer of oxide ion from the surface to the inside of molten oxide in the following stage. Based on the kinetic analysis of the oxygen exchange process, CO₂ dissociation rate constant, CO₂ re-formation rate constant and the mass transfer coefficient of oxide ion in molten oxides were calculated for the FeO_x-CaO and FeO_x-SiO₂ systems. Addition of CaO and SiO₂ to molten oxide increases and decreases the oxygen exchange reaction rate, respectively.

(cf. *ISIJ Int.*, **46** (2006), 974)

Influences of oxide additions on formation reaction of iron carbide at 1 023 K

G.LI *et al.*

The iron carbide was produced by reacting of iron ore fines with 70%H₂-30%CH₄ gas mixture at 1 023 K. The effects of 1 to 5 mass% MnO, Cr₂O₃, TiO₂ and V₂O₅ additives on iron carbide formation were experimentally investigated by gravimetric measurement. Phases formed during the reaction of iron carbide formation with and without oxide addition were examined by XRD, Mossbauer, and EDX analyses. The change of iron, iron oxides, and iron carbide compositions during reaction were quantitatively determined for samples added 1 mass% V₂O₅ and without oxide addition. The addition of Cr₂O₃ and MnO has no significant effect on the iron carbide formation. The TiO₂ addition retards both reduction of iron ore and iron carburization processes. Only 1 mass% V₂O₅ addition can enhance both reduction of iron ore and iron carburization reaction. The V₂O₅ addition also increases the conversion yields from iron ore to iron carbide to 96% The promotion of reduction and carburization by the addition of V₂O₅ may be caused by the enhancement of

catalytic effect of reduced metallic iron on methane cracking which can enhance both iron ore reduction and carburization.

(cf. *ISIJ Int.*, **46** (2006), 981)

Identification of titanium oxide phases equilibrated with liquid Fe-Ti alloy based on EBSD analysis

W.-Y.CHA *et al.*

There are huge quantities of uncertainties on the Ti deoxidation equilibrium constants and their interaction parameters in the literatures including the recommended values by the Japan Society for the Promotion of Science (JSPS). The main reason of such uncertainties among the previous works is due to the insufficient information of titanium oxide phase in equilibrium with liquid Fe-Ti alloy. The measurement of the equilibrium phase changes of titanium oxides with various Ti contents in molten Fe-Ti alloy has been carried out in the present study. Molten Fe-Ti alloys with various Ti contents have been equilibrated with 'Ti₃O₅' crucibles at 1 873 K. The kinds of Ti oxide at the interface of 'Ti₃O₅' crucible contacted with molten Fe-Ti alloys have been identified as the equilibrium titanium oxides with the electron backscatter diffraction (EBSD) pattern analysis technique. After the 'Ti₃O₅' crucible reacted with molten Fe-Ti alloys adequately and both of them were quenched.

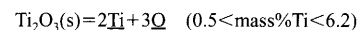
The present result on the stable region of equilibrium titanium oxides with Ti contents in Fe-Ti alloy was in good agreement with the thermodynamically calculated results based on the free energies of titanium oxides formation and the activity of Ti in Fe-Ti alloy.

(cf. *ISIJ Int.*, **46** (2006), 987)

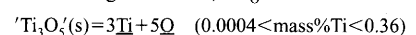
Equilibrium between titanium and oxygen in liquid Fe-Ti alloy coexisted with titanium oxides at 1 873 K

W.-Y.CHA *et al.*

The equilibrium between Ti and O has been investigated in molten Fe-Ti alloy saturated with various kinds of titanium oxides at 1 873 K. The present results have been thermodynamically analyzed applying Wagner's formalism as well as Darken's quadratic formalism with the excess Gibbs free energy change of mixing described by Redlich-Kister type polynomial. The equilibrium constants and the interaction parameters of Wagner's formalism were given as follows at 1 873 K in the present work.



$$\log K = -10.17, \quad e_{Ti}^O = -0.34$$



$$\log K = -16.86, \quad e_{Ti}^O = -0.34$$

The Henry constant of Ti in liquid Fe-Ti alloy was assessed as follows at 1 873 K.

$$\gamma_{Ti(l)}^O = 0.0090$$

The interaction parameters of Redlich-Kister type polynomial for molten Fe-Ti-O alloy were given by the following values at 1 873 K in the present work.

$${}^0\Omega_{Fe-Ti} = -73\,360/J$$

$${}^0\Omega_{Ti-O} = -1\,035\,900/J$$

The estimated results based on Wagner's formalism as well as Darken's quadratic formalism polynomials were well agreed with the experimental results which were observed between \bar{T}_i and \bar{Q} equilibrium contents in molten Fe-Ti alloy.

(cf. *ISIJ Int.*, **46** (2006), 996)

Ironmaking

Reducing ability of CO and H₂ of gases formed in the lower part of the blast furnace by gas and oil injection

S.SLABY et al.

Gases formed in the raceway by injection of reducing agents into the tuyere affect the blast furnace process in several ways. Energy set free by conversion in the raceway helps the melting of the burden and has beneficial effects on reaction kinetics. The formation of CO and H₂ helps to save blast furnace coke. The aim of this work is to study effects of the gases formed after the injection of coke oven gas (COG) and heavy oil into the tuyere of a blast furnace and after conversion in the raceway when entering the active coke zone. For this reason a gas conversion simulation is developed including description of the zones of the lower blast furnace part. The cases studied have the same melting rate at which the injection of COG is accomplished with one and two lances while those of oil is studied with one lance. The simulation predicts that the available amount of species for the reduction of iron ore and the reduction potential is similar for the studied reducing agents COG and heavy oil. Evaluating the potential to save coke a theoretical exchange ratio of 0.84 can be determined for comparable cases in terms of the same reduction progress so that the same consumption of coke has to be expected if no difference between the agents exists.

(cf. *ISIJ Int.*, **46** (2006), 1006)

Investigation on the dioxin emission from a commercial sintering plant

S.KASAMA et al.

Recent studies concerning the dioxin emission from the iron ore sintering process have clarified a dominant mechanism of dioxin formation and the substances to promote or to inhibit the reaction. In this paper, a detailed analysis of the exhaust gas at the Oita No.1 sintering plant has specified the strand positions where dioxins were released into the exhaust gas. The release of dioxins was detected at two different positions. The first release position was located at the point where the drying zone reached the hearth layer, showing a broad peak containing a large amount of furans. The second release position was located at the point where the melting zone reached the hearth layer, showing a sharp peak. Differences in dioxin congeners at the release positions imply a different mechanism of dioxin formation. The dioxins of the second release are considered to be formed in wind boxes at temperatures of 300°C or more. Controlling the burn through point to the discharge end is supposed to be effective for decreasing the dioxin emission in the second step.

(cf. *ISIJ Int.*, **46** (2006), 1014)

Properties of dust particles sampled from windboxes of an iron ore sintering plant: Surface structures of unburned carbon

N.TSUBOUCHI et al.

Aiming to understand the formation mechanism of dioxins in the iron ore sintering process, dust samples obtained from some windboxes of a commercial iron ore sintering plant have been characterized with a powder X-ray diffraction (XRD), by the transmission electron microscope (TEM) equipped with an electron energy loss spectroscopy (EELS), and by the temperature-programmed desorption (TPD) and temperature-programmed oxidation (TPO) techniques. The elemental and XRD analyses reveal that the content of the Cl present in the samples ranges from 0.075 mass%-dry to 5.1 mass%-dry and tends to be higher at smaller dust particles, and that some of the Cl exists as KCl with the average crystalline size between 40 nm and 50 nm. Dust samples also contain a significant amount of unburned carbon, and the smallest dust particles, <500 μm, show the highest C contents in many cases and consist partly of C, K, and Cl elements. The TPD and TPO experiments exhibit that the dust samples have several types of oxygen functional forms on the carbon surface, and the proportion of carboxyl and lactone/acid anhydride groups, which can be partly decomposed into CO₂ and carbon active sites at 150 to 500°C, tends to be larger at smaller dust particles. On the basis of the above results, the formation mechanism of chlorinated organic compounds including dioxins is discussed in term of interactions among HCl (and/or Cl₂), metallic chlorides, and carbon active sites.

(cf. *ISIJ Int.*, **46** (2006), 1020)

Analysis of exhaust gas visibility in iron ore sintering plant

S.KASAMA et al.

Visible smoke of exhaust gas from iron ore sintering plants spoil the scenery around the works. In this paper, the mechanism of formation of visible smoke is discussed by detailed analysis of the exhaust gas components and dust in the Oita No. 1 sintering plant. The main substance of visible smoke was mist condensing in the air during the cooling of exhaust gas that contained 0.1 ppm of sulfuric acid (SO₃). Sulfuric acid is considered to raise the dew point and so facilitate mist condensation, and to lower the vaporization of visible mist containing sulfuric acid solution. Dust in the exhaust gas is also considered to act as nucleation sites for mist condensation. This proposed mechanism was confirmed by the test remixing SO_x-rich gas with desulfurization gas in the Nagoya No. 3 sintering plant. Long trails of visible smoke were observed by remixing SO_x-rich gas with exhaust gas. In conclusion, in order to make exhaust gas invisible, it is not sufficient to enhance the dust collecting system: desulfurization equipment in the sintering plant is necessary.

(cf. *ISIJ Int.*, **46** (2006), 1027)

Casting and Solidification

Process for bimetallic slab of aluminium alloy under the level DC electromagnetic field

X.GAO et al.

In this paper, the EMBR technique was applied in producing the bimetallic slab on the basis of numerical simulation with the software of ANSYS. By suppressing the mixture of two kinds of molten metals in the mold of continuous casting strand with a level DC electromagnetic field, the bimetallic slab of Al-12wt%Si and Al-10wt%Mg was obtained. The slab was analyzed by XRD, EPMA and metallography. The results showed that there were same compositions on two sides of the slab obtained without electromagnetic field and there were different compositions on two sides of the slab obtained with electromagnetic field of 0.15 T, no obvious interface was found in the slab. The conclusion indicated that the electromagnetic field restrained the flow of the melt effectively.

(cf. *ISIJ Int.*, **46** (2006), 1033)

Prediction of tensile strength and elongation of high alloy steels during solidification

H.MIZUKAMI et al.

Phase dependence of tensile strength of high alloy steel during solidification has been studied by a technique for high temperature tensile testing. The experimental technique enabled a sample to melt and solidify without a crucible, and the measurement of a minute load in a solidification temperature range became possible. A numerical model for the analysis of phase transformation during solidification was developed with the assumption that local equilibrium holds at liquid/solid interface or δ/γ phase interface.

The zero strength temperature was in agreement with zero ductility temperature, and both of these temperatures appeared at the fraction solid of 0.8. Both the tensile strength and elongation of high alloy steel were dependent on the phase state but not on chromium and nickel contents. The tensile strength in (liquid+ δ), (liquid+ γ), (liquid+ δ + γ) and (δ + γ) coexisting state could be predicted using the experimental results. These estimated values are in good agreement with experimental results.

(cf. *ISIJ Int.*, **46** (2006), 1040)

Instrumentation, Control and System Engineering

Development of prediction method for abnormalities in slab continuous casting using artificial neural network models

W.XUDONG et al.

The breakout and other abnormalities in the mould have a critical influence on strand surface and casting productivity in continuous casting. Prediction of these mould abnormalities is an essential prerequisite for producing a good quality product with minimal disruption and defects. It is also important for optimization of casting process and oper-

ating safety. The mould friction (MDF) between strand and mould is one of the most important parameters that can be used to describe frictional behavior and mechanical interaction between the strand and the mould. Monitoring MDF online can contribute to evaluation of the powder lubrication, optimization of casting variables, prediction to breakout and other abnormalities. In this work, based on the measurement data of mould friction on two strands slab caster in a steel plant, the prediction method for MDF abnormalities has been investigated by using artificial neural network models in combination with two auxiliary algorithms, one for ramp and the other for pulse variation of MDF. A set of software to predict the MDF abnormalities of continuous casting has been developed. The results of simulating prediction for online measurement MDF data are found to be basically consistent with those collected from the abnormal records of steel plant.

(cf. *ISIJ Int.*, **46** (2006), 1047)

Chemical and Physical Analysis

Development of rapid analytical method of carbon in steels by glow discharge optical emission spectrometry

H. YASUHARA et al.

A rapid analytical method of carbon in steels by glow discharge optical emission spectrometry (GD-OES) was examined. The direct-current glow discharge was found to be more effective than the radio-frequency glow discharge for the analysis of carbon in steels because higher sputtering rates could be obtained in the direct-current glow discharge compared with the radio-frequency glow discharge. For the rapid and high precision simultaneous multi-elements analysis by GD-OES, the mechanism on a prolonged tailing of the emission intensity of carbon was investigated. We concluded that the contamination on the anode caused the gradual decrease in the emission intensity of carbon. The contaminant species could be removed more rapidly by use of the radio-frequency discharge associated with bias current conduction as a pre-burn discharge. The response time for the analysis of carbon was shortened and analytical repeatability of carbon was improved by using this new measurement program.

(cf. *ISIJ Int.*, **46** (2006), 1054)

Forming Processing and Thermomechanical Treatment

Effect of thermomechanical controlled processing on the microstructure and mechanical properties of Fe-C-Mn-Si multiphase steels

D. WU et al.

In this paper, a three step cooling (first water cooling, subsequent air cooling and second water cooling stage) pattern on the runout table (ROT) was conducted in a laboratory hot rolling mill, and effect of thermomechanical controlled processing (TMCP) on the microstructure and mechanical properties of Fe-C-Mn-Si multiphase steels was investigated. The results showed that the microstructure containing polygonal ferrite, granular bainite

and a significant amount of the stable retained austenite can be obtained through three step cooling on the ROT after hot rolling. The first water cooling stage made high density dislocation remain in the austenite, the second water cooling stage avoided pearlite formation, and it is necessary to hold about 10 s during intermediate air cooling on the ROT, which contributes to enhancement the stability of retained austenite. Excellent mechanical properties were obtained through TMCP due to the transformation of retained austenite into martensite during straining (transformation induced plasticity) for the present Fe-C-Mn-Si multiphase steels, and the specimen 3 shows the highest value of total elongation (37%) and the balance of strength and ductility (30488 MPa%).

(cf. *ISIJ Int.*, **46** (2006), 1059)

Surface Treatment and Corrosion

Evaluation of the hot corrosion behavior of LPG assisted HVOF NiCr wire sprayed boiler tube steels in molten salt environments

H.S. SIDHU et al.

NiCr coatings were deposited on some boiler tube steels by High Velocity Oxy Fuel spraying process using LPG as fuel gas. Hot corrosion behaviour of uncoated as well as HVOF sprayed specimens was studied in an environment of Na_2SO_4 -60% V_2O_5 at 900°C under cyclic conditions. The thermogravimetric technique was used to establish the kinetics of corrosion. SEM/EDAX, XRD and EPMA techniques were used to analyse the corrosion products. The NiCr coating found to be very effective in decreasing the corrosion rate of the uncoated steels. The NiCr coated samples showed no cracking or spalling of oxide scale during hot corrosion. The formation of protective oxide scale as observed may be contributing to the development of hot corrosion resistance in the coatings studied, which mainly consists of oxides of NiO, NiCr_2O_4 and Cr_2O_3 .

(cf. *ISIJ Int.*, **46** (2006), 1067)

Corrosion resistance of Cr-bearing rebar in concrete with chloride ion content

S.-H. TAE et al.

As a fundamental study on the performance of Cr-bearing rebars in steel reinforced concrete structures exposed to corrosive environments, The test specimens were made by installing 8 types of rebars in concretes with a chloride ion content of 0.3, 0.6, 1.2, 2.4 and 24 kg/m³. Corrosion accelerated curing were then conducted with them. The corrosion resistance of Cr-bearing rebars was examined by measuring crack widths, half-cell potential, corrosion area and weight loss after 155 cycles of corrosion-accelerating curing.

The results of the study showed that the corrosion resistance increased as the Cr content increased regardless of the content of chloride ions, and that the Cr-bearing rebars with a Cr content of 5% and 9% showed high corrosion resistance in concretes with a chloride ion content of 1.2 and 2.4 kg/m³, respectively.

(cf. *ISIJ Int.*, **46** (2006), 1075)

Hydrogen entry in crevice region: evaluation by hydrogen permeation technique

T. SUNDARARAJAN et al.

Pure iron exposed to acetate buffer showed both metal dissolution and hydrogen evolution inside the crevice region. Potential drop occurred inside the crevice led to both active dissolution and cathodic reactions. Hydrogen ingress into the specimen was monitored on the rear side using electrochemical hydrogen permeation technique. The results showed that magnitude of hydrogen entered inside the crevice could be detected by the permeation technique. Change in the applied potential significantly influenced the amount of permeated hydrogen. The results are correlated potential drop occurred inside the crevice, which influenced the magnitude of diffusable hydrogen.

(cf. *ISIJ Int.*, **46** (2006), 1081)

Corrosion resistance of Cr-bearing rebar to macrocell corrosion caused by concrete cover crack

S.-H. TAE et al.

Artificial cracks were made in the cover concrete of specimens embedding ten types of steel rebars having different Cr contents with the aim of developing Cr-bearing steel rebars resistant to macrocell corrosion environments induced by cracking in cover concrete. The cracks were subjected to intensive penetration of carbon dioxide (carbonation specimens) and chloride ions (chloride attack specimens) to form macrocells. Both groups of specimens were then subjected to accelerated corrosion curing, during which the macrocell corrosion current density was measured. The corrosion area and corrosion loss were also measured at the end of 105 cycles of this accelerated curing. In a macrocell corrosion environment induced by localized carbonation, the minimum Cr content of rebars required for corrosion resistance was 7%. Rebars with a Cr content of 11% were proven corrosion-resistant in a chloride ion concentration macrocell with a concentration difference of not more than 3 kg/m³.

(cf. *ISIJ Int.*, **46** (2006), 1086)

Transformations and Microstructures

Influence of deformation and molybdenum content on acicular ferrite formation in medium carbon steels

C. CAPDEVILA et al.

The present work deals with the influence of deformation and molybdenum content on the subsequent austenite-to-acicular ferrite transformation during continuous cooling in medium carbon microalloyed steels. The results obtained demonstrate that higher deformation temperature induces a finer austenite grain size as a result of austenite recrystallisation processes during cooling down to austenite decomposition temperature. The higher the molybdenum content and severity of deformation are, the finer austenite grain is. Likewise, it was concluded that molybdenum suppress pearlitic microstructure, and clearly delay proeutectoid ferrite

field to longer times. By contrast, acicular ferrite transformation is enhanced in molybdenum rich steel, which not only affect the volume fraction but also the morphology of acicular ferrite.

(cf. *ISIJ Int.*, **46** (2006), 1093)

Mechanical Properties

Microstructure and dry sliding wear behaviour of cast Al-8%Si-0.3%Mg alloy against En-31

D.K. DWIVEDI

In present paper, the influence of sliding speed, contact load, sliding time and silicon content on interface temperature and wear behaviour during the sliding of cast Al-8%Si-0.3%Mg alloy in as cast, melt treated and heat treated conditions has been re-

ported. Dry sliding tests were conducted against hardened steel En-31 counter surface (RC 60) at a constant normal load (30 N) over a range of sliding speed from 0.3 to 4.0 m/s. It was observed that the interface temperature and wear rate is a function of sliding speed and sliding distance. The wear of alloys under investigation has a close relationship with interface temperature. There is a critical temperature at which the transition from mild to severe wear takes place.

(cf. *ISIJ Int.*, **46** (2006), 1101)